

Optimal spectral reshaping for resolution improvement in optical coherence tomography

Jianmin Gong, Bo Liu, Young L. Kim, Yang Liu, Xu Li, Vadim Backman

Biomedical Engineering Department, Northwestern University, IL 60208, USA

j-gong@northwestern.edu

Abstract: We analyze the resolution limit that can be achieved by means of spectral reshaping in optical coherence tomography images and demonstrate that the resolution can be improved by means of modelessly reshaping the source spectrum in postprocessing. We show that the optimal spectrum has *a priori* surprising “crater-like” shape, providing 0.74 micron axial resolution in free-space. This represents ~50% improvement compared to resolution using the original spectrum of a white light lamp.

©2006 Optical Society of America

OCIS codes: (100.2980) Image enhancement; (170.4500) Optical coherence tomography; (350.5730) Resolution

References and links

1. D. Huang, E. A. Swanson, C. P. Lin, J. S. Schuman, W. G. Stinson, W. Chang, M. R. Hee, T. Flotte, K. Gregory, C. A. Puliafito, and J. G. Fujimoto, “Optical coherence tomography,” *Science*, **254**, 1178 (1991).
2. Brett E. Bouma, Guillermo J. Tearney, *Handbook of optical coherence tomograph*, (Marcel Dekker, New York, 2002)
3. B. Bouma, G. Tearney, S. Boppart, M. Hee, M. Brezinski, and J. Fujimoto, “High-resolution optical coherence tomographic imaging using a mode-locked Ti:Al₂O₃ laser source,” *Opt. Lett.* **20** 1486-1488 (1995)
4. B. Povazay, K. Bizheva, A. Unterhuber, B. Hermann, H. Sattmann, A. F. Fercher, W. Drexler, A. Apolonski, W. J. Wadsworth, J. C. Knight, P. St. J. Russell, M. Vetterlein and E. Scherzer, “Submicrometer axial resolution optical coherence tomography,” *Opt. Lett.* **27** 1800-1802 (2002)
5. Wolfgang Drexler, “Ultrahigh-resolution optical coherence tomography,” *J. Biomed. Opt.* **9**, 47–74 (2004)
6. A. Dubois, G. Moneron, K. Grieve and A.C. Boccara, “Three-dimensional cellular-level imaging using full-field optical coherence tomography,” *Phys. Med. Biol.* **49** 1227–1234 (2004)
7. A. Wax, C.H. Yang, J.A. Izatt, “Fourier-domain low-coherence interferometry for light-scattering spectroscopy,” *Opt. Lett.* **28** 1230-1232 (2003)
8. Yan Zhang and Manabu Sato, “Resolution improvement in optical coherence tomography by optimal synthesis of light-emitting diodes,” *Opt. Lett.* **26**, 205-207 (2001)
9. Renu Tripathi, Nader Nassif, J. Stuart Nelson, Boris Hyle Park and Johannes F. de Boer, “Spectral shaping for non-Gaussian source spectra in optical coherence tomography,” *Opt. Lett.* **27**, 406-408 (2002)
10. E. Smith, S. C. Moore, N. Wada, W. Chujo, and D. D. Sampson, “Spectral domain interferometry for OCDR using non-Gaussian broadband sources,” *IEEE Photon. Technol. Lett.* **13**, 64-66 (2001)
11. A. Ceyhan Akcay, Jannick P. Rolland and Jason M. Eichenholz, “Spectral shaping to improve the point spread function in optical coherence tomography,” *Opt. Lett.* **28**, 1921-1923 (2003)
12. Daniel Marks, P. Scott Carney, Stephen A. Boppart, “Adaptive spectral apodization for sidelobe reduction in optical coherence tomography images,” *J. Biomed. Opt.* **9**, 1281-1287 (2004)
13. T.F. Coleman, and Y. Li, “A Reflective Newton Method for Minimizing a Quadratic Function Subject to Bounds on Some of the Variables,” *SIAM J. Optimiz.* **6**, 1040-1058 (1996)

1. Introduction

Optical coherence tomography is a promising non-invasive *in vivo* imaging technique, which has undergone rapid development since its invention in 1991 [1,2]. In an OCT system, the axial resolution is determined by the temporal coherence length l_c of a light source. If the spectrum of the light source has a Gaussian shape, l_c is proportional to $\lambda_0^2/\Delta\lambda$ with λ_0 the

central wavelength and $\Delta\lambda$ the bandwidth of the emission spectrum, respectively [2]. Depending on the choice of a light source, the axial resolution of a typical OCT system varies from ~ 1 to $30 \mu\text{m}$. Several techniques have been proposed to improve the resolution of OCT. One possible strategy is to develop new light sources with shorter coherence lengths. For example, a Kerr-lens mode-locked Ti:sapphire laser [3], Ti:sapphire pumped super-continuum [4,5], and thermal light sources [6,7] were used to obtain 3.7 [3], 0.5 [4], ~ 1 [5], 0.7 [6], and $\sim 1 \mu\text{m}$ [7] axial resolution in biological tissue, respectively. Alternatively, resolution can be improved by combining multiple light sources, e.g. after optimizing the power ratios of three LEDs, resolution in OCT images was improved from $12 \mu\text{m}$ to $7 \mu\text{m}$ [8]. Moreover, by digitally reshaping the source spectra to known modes, such as Gaussian, white, and Hamming windowed shapes, OCT resolution was enhanced from over 10 to a few microns [9,10,11]. A modeless spectral reshaping, in which a spectral profile can be changed to any arbitrary shape, was used to effectively reduce sidelobes of in OCT images [12].

In this Letter we analyze the resolution limit that can be achieved by means of the modeless spectral reshaping approach, determine the shape of the optimal spectrum, and use this to improve the resolution of OCT.

2. Theory and simulation

The modeless spectral reshaping we propose here is based on a spectral domain OCT modality in which the interference signal $I(k, r)$ is given by [2]

$$I(k, r) = P(k)Q(k) \left| R^{1/2}(k) \exp[2ik(z_0 + r)] + S^{1/2}(k) \int_0^\infty a(z) \exp[2ik(z_0 + nz)] dz \right|^2 \quad (1)$$

$$= P(k)Q(k) \{ R(k) + S(k)B + [R(k)S(k)B]^{1/2} I_d(k, r) \}$$

where $k=2\pi/\lambda$ is the wave number; n is the refractive index of the sample; z_0 is the path length from the beam splitter to the top surface of the sample, z is the depth of the sample, r is the path difference between the reference mirror and the top surface of the sample; $a(z)$ is the depth-resolved backscattered amplitude of the sample; $P(k)$, $Q(k)$, $R(k)$ and $S(k)$ are the source spectrum, spectral response of the detector, reflection spectrum of the reference mirror, and the scattering spectrum in the sample (dispersion within the sample was neglected), respectively; $B \equiv \int_0^\infty \int_0^\infty a(z)a(z') \exp[2ink(z-z')] dz dz'$ describes the mutual interference of the light scattered from the sample; $I_d(k, r) = 2 \int_0^\infty a(z) \cos 2k(r-nz) dz / B^{1/2}$ decodes the depth-resolved OCT signal from the sample $a(z)$, which we aim to obtain. In an experiment, by blocking the reference or sample arm, respectively, $P(k)Q(k)S(k)B$ and $P(k)Q(k)R(k)$ can be recorded, and $I_d(k, r)$ can then be obtained as

$$I_d(k, r) = [I(k, r) - PQR - PQSB] / [(PQR) \times (PQSB)]^{1/2}. \quad (2)$$

The bandwidth of an OCT system is limited by the spectrum of a light source as well as the spectral range of the detector and other components. Assuming that the minimum and maximum detectable wave numbers are k_1 and k_2 , respectively, the sum of the interference signal weighted with a distribution $V(k)$ within the range $[k_1, k_2]$ can be expressed as follows:

$$I_d(r) = \int_{k_1}^{k_2} V(k) I_d(k, r) dk = 2 \int_0^\infty a(z) \text{PSF}(Z) dz / B^{1/2} \quad (3)$$

where

$$\text{PSF}(Z) \equiv \text{PSF}(r-nz) \equiv \int_{k_1}^{k_2} V(k) \cos 2k(r-nz) dk \quad (4)$$

is the point spread function (PSF) that determines axial resolution and $V(k)$ can be reshaped in postprocessing. In order to improve the resolution, the width of PSF has to be minimized.

Equation (4) can be rewritten as

$$\text{PSF}(Z) = \int_0^\infty \tilde{V}(k) \text{rect}(k_1, k_2) \cos 2kZ dk = [\int_0^\infty \tilde{V}(k) \cos 2kZ dk] \otimes U(Z) \quad (5)$$

where \otimes denotes convolution operation, $\text{rect}(k_1, k_2)$ is the rectangle function which equals to 1 within the range $[k_1, k_2]$ and zero elsewhere, and

$U(Z) = \pi(k_2 - k_1) \cos[(k_1 + k_2)Z] \text{sinc}[(k_2 - k_1)Z] / 4$ is a high frequency oscillation term whose envelope is a sinc function. If $V(k)$ is a constant (i.e. white light source), the first term in Eq. (5) would be a delta function, and PSF would equal to $U(Z)$. The peak of this PSF is narrow; however the sidelobes are large. If $V(k)$ is Gaussian or Hamming windowed, the sidelobes can be significantly compressed, however the peak of the PSF is broadened. In this paper we optimized $V(k)$ so that $U(Z)$ functions with different shifts compensate each other to create a narrower PSF peak than that of white light, at the same time the sidelobes are suppressed to a lower level than that of white light also.

It is hard to get an analytical solution for the optimal spectrum $V(k)$. We discretize the optical path difference (OPD) and wave number as Z_i ($i=1, 2, \dots, M$) and k_j ($j=1, 2, \dots, W$), respectively, and rewrite Eq. (5) in matrix notations:

$$\begin{pmatrix} f_1 \\ f_2 \\ \vdots \\ f_M \end{pmatrix} = \begin{bmatrix} g_{11} & g_{12} & \cdots & g_{1W} \\ g_{21} & g_{22} & \cdots & g_{2W} \\ \vdots & \vdots & \ddots & \vdots \\ g_{M1} & g_{M2} & \cdots & g_{MW} \end{bmatrix} \begin{pmatrix} v_1 \\ v_2 \\ \vdots \\ v_W \end{pmatrix} \text{ or } F=GV, \quad (6)$$

where f_i is the PSF for Z_i , $v_j=V(k_j)$, and $g_{ij} = \cos 2k_j Z_i$. In order to find the optimal spectrum V , we solved the nested optimization problem: $\min_F FWHM(GV)$ and $\min_v \|GV - F\|_2^2$, where $FWHM$ represents the full-width half-maximum. The optimization procedure is shown as Fig. 1. Since the shape of the PSF of a broad-band source is similar to the sinc function, we selected the sinc function with a variable width T , $\text{sinc}(Z/T)$, as the target PSF. The initial width T was set to $1/k_1$. In the m -th iteration, the target function F_m was chosen as $\text{sinc}(Z/T_m)$, the half-optimal spectrum V_m was found so that $\|GV_m - F_m\|_2^2$ is minimal, and the FWHM of its corresponding PSF, D_m , was calculated by Hilbert transform. In order to optimize F , we applied a 0.1% perturbation to T_m to obtained another FWHM D_m' , and in the following iteration, T_m was set as $T_{m-1} + \gamma(D_{m-1} - D_{m-1}')$ to give a PSF with narrower peak. γ is a proportional coefficient. Normally a smaller value of γ leads to more stable convergence but also increases the complexity of computations. In our computations, the convergence criterion was set as $\gamma(D - D') < 10^{-5} T_m$, and γ was chosen as 10 to ensure the convergence after 100-1000 iterations. The reflective Newton iterative method [13], which allows setting the range of v_j , was chosen to solve the matrix-form least-squares problem, and set the lower limit of v_j to zero to satisfy the physics of real light sources. The system is spectrally sensitive, and the signal-to-noise ratio (SNR) values differ significantly at different wave numbers. In order to limit the use of noisy spectral data, we applied an additional condition $\sum_{w=1}^W v_w / SNR_w < \alpha$ for

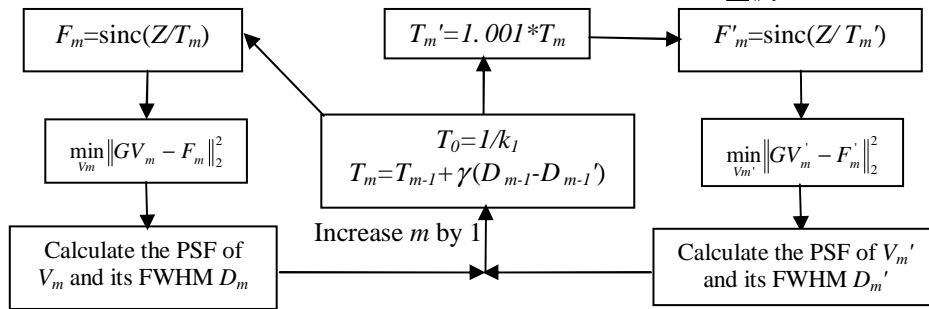


Fig. 1. PSF optimization algorithm

the optimization, where SNR_w is the signal-to-noise ratio at wave number v_w which was obtained by dividing the signal level at wave number v_w by the amplitude of background white noise. α is a threshold controlling the trade-off of the SNR and the FWHM. For a less α

value, the SNR has larger effect while FWHM has lower effect on the optimization procedure. After a few attempts we selected α as W , the number of the wave numbers.

The obtained optimal spectrum was shown in Fig. 2. Different from the conventional symmetric bell-like reshaping spectrum, the optimal spectrum has *a priori* surprising asymmetric crater-like shape with two peaks close to the lower and upper bounds of the spectrum, and the peak at shorter wavelength is higher. It can be understood with this way: the resolution is primarily limited by the shortest and longest detectable wavelengths, especially the shortest detectable wavelength, so the side-spectrum enhancement, especially the enhancement at the shorter wavelength side, helps improve the resolution. In Fig. 2 we also show five other spectra: the modified optimal spectrum which is more symmetric with the amplitude of the two peaks being the same, Gaussian profile with FWHM = 300 nm, white light, white light weighted with Hamming window, and the xenon lamp spectrum. To be consistent with our experimental system, a wavelength band from 421 nm to 895 nm was used. The envelopes of theoretical PSFs of the six spectra are shown in Fig. 4(a), and their

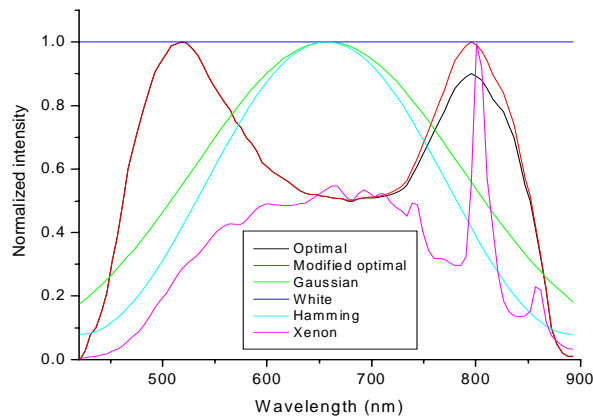


Fig. 2. Typical light source spectra

FWHM values are given in the notation text. Evidently, the optimal spectrum provides the highest FWHM resolution, 0.44 μm in free space, with sidelobes lower than those of the PSF generated by the white light spectrum. The PSF peak of the modified optimal spectrum is slightly broader than that of the optimal spectrum, which proves that an asymmetric spectral profile may lead to a higher resolution than a symmetric spectral profile. To quantitatively compare the sidelobes effect of the PSFs, we calculated the root-mean square width (RMSW) $[\int z^2 |PSF(z)|^2 dz / \int |PSF(z)|^2 dz]^{1/2}$ which represents the deviation of the PSF from the central position $z=0$ [12]. The theoretical FWHM and RMSW values are shown in Table 1. the optimal spectrum provides the highest FWHM as well as adequate RMSW.

Table 1. Optimal PSF has improved FWHM and RMSW compared to other PSF given by white light, Gaussian, and Hamming windowed spectra

Properties Spectra	From Theory		From Experiments	
	FWHM (μm)	RMSW (μm)	FWHM (μm)	RMSW (μm)
Xenon	1.18	1.05	1.51	1.12
Gaussian	0.70	0.33	1.06	0.37
Hamming	0.82	0.29	1.03	0.37
White Light	0.52	0.89	0.92	0.67
Optimal	0.44	0.60	0.74	0.50

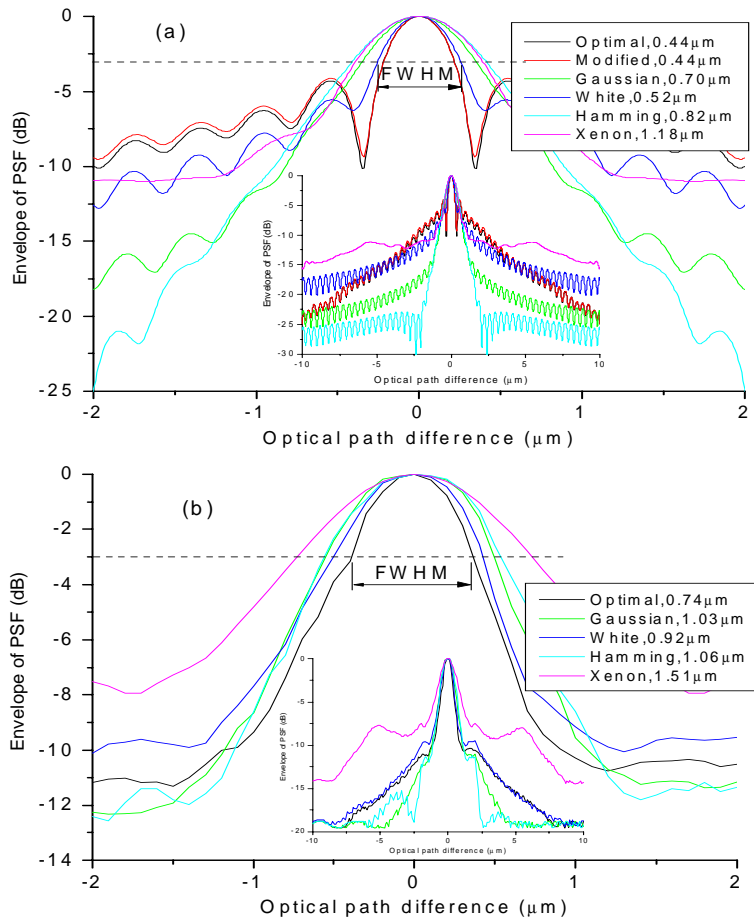


Fig. 3. The optimal PSF provides improved OCT resolution for the source spectra shown in Fig. 3. (a) Envelopes of theoretical PSFs (b) Envelopes of experimentally measured PSFs. PSFs in the insets are normalized to conserve the L2 norm.

3. Experimental results

The approach reported in section 2 was also validated experimentally. Our spectroscopic OCT system setup is shown in Figure 4. A 250W xenon lamp (Oriel) was used as the light source. The output of the xenon lamp was first collimated by two 250-mm-focal-length lenses L1 and L2 together with a 1 mm pinhole, spatially filtered by an adjustable aperture, and then separated into the reference and sample beams by a polarization independent beam splitter BS. We used the largest facet of an uncoated right-angle prism as the reference mirror M1. Two identical 4x achromatic objective lenses were used to focus the light beams to M1 and the sample, and collected the light back reflected/scattered by M1 and the sample. The collected light was analyzed by means of a spectrograph (Acton SP2150i) coupled into a CCD camera (Princeton instruments PIMAX 1KHQ), and magnification of the sample to the CCD was 20. The width of the entrance slit of the spectrograph was adjusted to be $10\mu\text{m}$, that is, the vicinity of $10/20=0.5\mu\text{m}$ of the reference mirror or the sample was regarded as a single dot light from the . The detection system was sensitive to wavelengths from 421nm to 895 nm, with a spectral resolution of 2 nm. When biological tissue was used as a sample, the CCD was

set to a higher gain and longer integration time, and in order to avoid the CCD saturation, a neutral density filter with 10 dB single-trip loss was inserted in the reference arm. A glass was placed in the sample arm to compensate the additional optical path introduced by the neutral density filter. Reference mirror M1 and lens L3 were moved as one unit to change the OPD between the reference and sample beams with a step size of $0.1 \mu\text{m}$. Interference spectrum $I(\lambda, r)$ was recorded at each OPD step. For calibration, $I(\lambda, r)$ reflected by the reference mirror and the sample were also recorded at both the beginning and the end of each imaging experiment. We then followed Eq. (2) to obtain $I_d(k, r)$ for different k and r values, and applied different spectra $V(k)$ to get the corresponding $I_d(r)$ values according to Eq. (3).

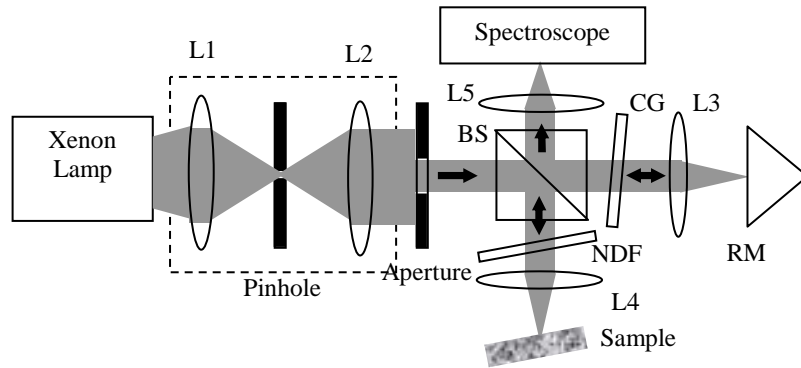


Fig. 4. Schematic of a spectral domain OCT system: BS, beam splitter; NDF, neutral density filter; PCG, phase compensation glass; RM, reference mirror

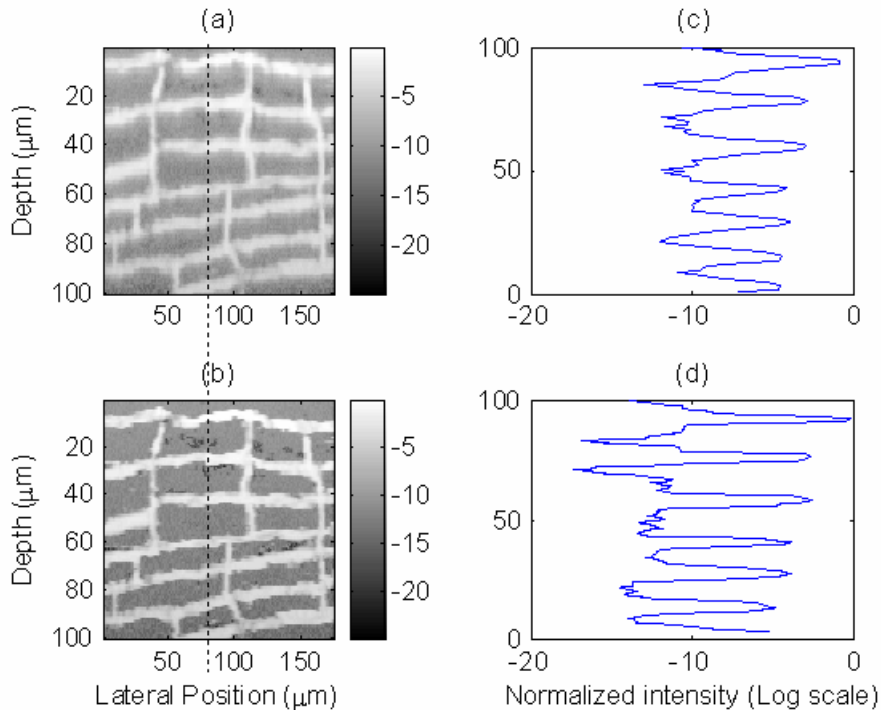


Fig. 5. OCT images of an onion root tip tissue (a) Image obtained with the originally detected xenon spectrum. (b) Image obtained with the optimal spectrum. (c) Intensity cross section from the image shown in panel (a) at lateral position $80 \mu\text{m}$. (d) Intensity cross section from the image shown in panel (b) at lateral position $80 \mu\text{m}$.

A piece of microscope cover glass was used as the sample first. The light was focused on the top surface of the glass and $a(z)$ can be regarded as a delta function. Thus the resulted $I_d(r)$ gave the PSFs for different source spectra $V(k)$. Fig. 3(b) shows the envelope of the experimental PSFs. There are multi-peaks in the theoretical PSF, with about 100nm between the adjacent peaks. In the experiments, the un-flatness of components surfaces and the dispersion induced optical path mismatch, which are in the order of 100nm, smooth the peaks. So there is no multiple peaks in the experimental PSFs. The corresponding FWHM and RMSW values are given in Table 1. As shown in Fig. 3(b) and Table 1, the modeless spectral reshaping indeed provides resolution superior to those obtained with other conventionally used spectra including the original xenon-lamp spectrum, white light, Gaussian spectrum, and Hamming windowed profile, with the FWHM reduced by 51%, 20%, 28%, and 30%, respectively. Although the spectrum was not purposely reshaped to optimize the sidelobes, we also notice that the optimal spectrum suppress sidelobes compared to the original xenon-lamp spectrum with RMSW reduced by 54%. The sidelobes are larger, however, than those of corresponding to the Gaussian and Hamming profiles.

As a further illustration of the improved resolution, some onion root tip tissue was used the sample. The experiment was repeated by 100 times, and the results were averaged to give a higher SNR. Figs. 5(a, b) show the B-scan images before and after spectral reshaping, respectively, and Figs. 5(c, d) show the corresponding A-scan traces taken from the images at 75 μm lateral position. Evidently, the image/trace obtained using the optimal spectrum (Figs. 5(b, d)) has an improved higher resolution compared to those obtained using the original xenon-lamp spectrum (Figs. 5(a, c)).

4. Conclusions

In summary, we showed that the optimal spectrum has *a priori* surprising crater-like spectral shape, which is different from the conventionally adopted bell-shape spectra. Although the resolution provided by the optimal spectrum is primarily determined by the spectral range, we further demonstrated, for the first time to our knowledge, the optimal spectral reshaping results in an extra improvement in resolution. In particular, in our experiments, the resolution of 0.74 μm in free space was obtained, which is 51% higher than the one provided by the original xenon-lamp spectrum. Therefore, the modeless spectral reshaping technique provides a flexible way to improve the resolution of OCT and may help achieve sub-micron resolution for subcellular OCT imaging.

Acknowledgments

This work is supported by NIH grants R01CA112315, R01EB003682, and a grant from the Wallace H. Coulter Foundation.